High-throughput combinatorial approach expedites the synthesis of a lead-free relaxor ferroelectric system

Di Zhang¹*, Katherine Harmon², Michael J. Zachman³, Ping Lu⁴, Doyun Kim⁵, Zhan Zhang⁶, Nickolas Cucciniello¹, Reid Markland¹, Ken William Ssennyimba¹, Hua Zhou⁶, Yue Cao², Matthew J. Brahlek⁷, Hao Zheng^{2,6}, Matthew M. Schneider⁸, Alessandro R. Mazza^{1,8}, Zach Hughes¹, Chase Somodi¹, Benjamin Freiman¹, Sarah Pooley¹, Sundar Kunwar¹, Pinku Roy¹, Qing Tu⁵, Rodney J. McCabe⁸, Aiping Chen¹*

¹ Dr. D. Zhang, N. Cucciniello, R. Markland, K.W. Ssennyimba, Dr. A. R. Mazza, Z. Hughes, C. Somodi, B. Freiman, S. Pooley, Dr. S. Kunwar, Dr. P. Roy, Dr. A. P. Chen Center for Integrated Nanotechnologies
Los Alamos National Laboratory
Los Alamos, NM 87545, USA
Email: dizhang@lanl.gov, apchen@lanl.gov

² Dr. K. Harmon, Dr. Y. Cao, Dr. H. Zheng Materials Science Division Argonne National Laboratory Lemont, IL 60439, USA

³ Dr. M. J. Zachman Center for Nanophase Materials Sciences Oak Ridge National Laboratory Oak Ridge, TN 37830, USA

⁴ Dr. P. Lu Sandia National Laboratories Albuquerque, NM 87185, USA

⁵ Dr. D. Kim, Dr. Q. Tu Department of Materials Science and Engineering Texas A&M University College Station, TX 77840, USA

⁶ Dr. Z. Zhang, Dr. H. Zhou, Dr. H. Zheng Advanced Photon Source (APS) Argonne National Laboratory Lemont, IL 60439, USA

⁷ Dr. M. J. Brahlek
 Materials Science and Technology Division
 Oak Ridge National Laboratory

Oak Ridge, TN 37830, USA

⁸ M. M. Schneider, Dr. A. R. Mazza, Dr. R. J. McCabe Materials Science and Technology Division Los Alamos National Laboratory Los Alamos, NM 87545, USA

Abstract

Developing novel lead-free ferroelectric materials is crucial for next-generation microelectronic technologies in regard to clean energy and environmental sustainability. However, materials discovery and property optimization are typically time-consuming due to the limited throughput of traditional synthesis methods. In this work, we use a high-throughput combinatorial synthesis approach to fabricate lead-free ferroelectric superlattices and solid solutions of (Ba_{0.7}Ca_{0.3})TiO₃ (BCT) and Ba(Zr_{0.2}Ti_{0.8})O₃ (BZT) phases with continuous variation of composition and layer thickness. High-resolution X-ray diffraction (XRD) and scanning transmission electron microscopy (STEM) demonstrate high film quality and well-controlled compositional gradients. Ferroelectric and dielectric properties identify the "optimal property point" achieved at the morphotropic phase boundary (MPB) with a composition of 48BZT-52BCT. Displacement vector maps reveal that ferroelectric domain sizes are tunable by varying {BCT-BZT}_N superlattice geometry. This high-throughput synthesis approach can be applied to many other material systems to expedite new materials discovery and properties optimization – allowing for the exploration of a large area of phase space with a single growth.

Introduction

Traditional lead-based ferroelectrics such as lead zirconate titanate Pb(Zr_xTi_{1-x})O₃ (PZT), though exhibiting outstanding piezoelectric properties, are not viable in many applications as processes

including lead (Pb) have a negative effect on the environment and human health. Hence, lead-free ferroelectrics have been the subject of considerable research interest in recent decades. Tremendous effort has been devoted to improving the piezoelectricity, energy storage density and efficiency of lead-free dielectric systems (1-3). BaTiO₃ (BTO)-based perovskite ferroelectric oxides are one of the most studied and widely used lead-free ferroelectric systems owing to their non-toxicity, simple fabrication process, and thermal and mechanical stabilities (4, 5). By substituting Ba²⁺ (A site) or Ti⁴⁺ (B site) ions in BaTiO₃ with other transition metal ions to form a variety of stable compositions including (Ba_{1-x} M_x)TiO₃ (M = Na, K, Ca, Sr, etc.) and Ba(N_y Ti₁₋ $_{\rm v}$)O₃ ($N = {\rm Zr}$, Sn, Nb, Mn, etc.), the ferroelectric properties such as polarization, domain configuration, and coercivity can be remarkably tuned in these solid state solutions (6-9). In particular, the BTO-based relaxor ferroelectrics at their morphotropic phase boundary (MPB) compositions have been reported to show ultra-high piezoelectricity and efficiency of energy storage and conversion, making them ideal candidates for applications in non-volatile memory, neuromorphic computing, and energy storage devices (10-12). Consequently, the effect of various dopants on the ferroelectric properties of BTO-based systems has been intensively studied in recent years (13-15). However, specimens produced by conventional synthesis methods often contain fixed dopant levels, compositions, and geometries as reported in thin films, heterostructures, superlattices, and nanocomposites (16), making materials discovery across large chemical and geometric spaces challenging. Furthermore, unavoidable sample-to-sample variation introduces uncertainties into measured properties, which lessens the accuracy of systematic studies and reduces data reliability in material informatics.

High-throughput combinatorial synthesis approaches can accelerate new materials discovery by facilitating efficient identification of optimal functional properties (17-19). This is accomplished

by rapidly surveying a large compositional landscape via synthesizing samples with a continuous compositional spread in a single experimental growth. In addition, the continuous variation of the local chemistry or geometry allows for a finer tuning of the composition as compared to conventional mix-and-measure approaches. Subsequent location-dependent structural characterization and property measurements then enable the creation of a "structure-property correlation map," which allows identifying the composition of a region with optimal properties. This high-throughput synthesis concept has enabled rapid discovery of new optical, electrical, magnetic, and structural materials (20-23). Using such a technique to expedite the discovery of relaxor ferroelectric thin films for energy storage is essential as there are large unexplored elemental and geometric spaces for these materials systems.

In this work, we use a high-throughput combinatorial pulsed laser deposition (cPLD) approach to expedite the exploration of film geometry and composition effects on ferroelectric properties in lead-free (Ba_{0.7}Ca_{0.3})TiO₃ (BCT) and Ba(Zr_{0.2}Ti_{0.8})O₃ (BZT)-based superlattices and thin films. To investigate the effect of SL geometry (*e.g.*, number of layers and interlayer thickness) and composition on the ferroelectric properties, we grow three series of BCT-BZT SL films with different numbers of layers while keeping the total film thicknesses nearly constant. High resolution X-ray diffraction (XRD) and scanning transmission electron microscopy (STEM) experiments are conducted to reveal the epitaxial growth quality and microstructure of the BCT-BZT films. By systematically measuring ferroelectric properties of all samples, we establish "structure-property library maps" across different film geometries. Via analyzing polarization displacement vector maps, we further show that both the composition ratio and the geometry controlled polar domain size play critical roles in determining the properties of these films.

Results

Growth of BCT-BZT films

As illustrated in Figures 1A-B, BCT and BZT targets (see methods for details) are used in the thin film deposition. Five identically sized ($5\times10 \text{ mm}^2$) STO (001) substrates coated with $\sim60 \text{ nm}$ thick SrRuO₃ (SRO) buffer layer, named from "A" to "E", are placed side by side on the substrate plate. During deposition, the substrate plate is kept static while the targets are rotated. The films studied here are grown by the following process. In "Phase 1" (Figure 1A), the BZT target is placed onaxis with substrate A so that the growth rate on substrate A (E) is the highest (lowest), leading to a thickness gradient from substrate A (thickest) to E (thinnest). In "Phase 2" (Figure 1B), the substrate plate is rotated in addition to the target position such that substrate E is placed on-axis with the BCT target. In this case, the thickness gradient of BCT is opposite to that of the BZT deposited in Phase 1 such that the BCT layer on substrate E (E) is the thickest (thinnest). By alternating repeatedly between "Phases 1 & 2" during the deposition process, thin films with either a BZT-BCT superlattice (SL) structure or a solid solution structure are created. These films have a location-dependent SL geometry (E, periodic BCT-BZT layers) and/or composition gradient. Therefore, both geometry and composition tuning are achieved via a simple process.

Figure 1C shows schematic cross-sectional views of the three $\{xBCT-(1-x)BZT\}_N$ (N=40,80,240) thin film series grown using the cPLD technique. Each series has 5 samples, labeled A to E, yielding a total of 15 samples across the three series. x represents the composition of BCT, which is location dependent. In other words, x changes continuously from A to E. Samples are defined herein by the letter 'S' followed by the number of layers N and the letter A-E of the sample within its series. For example, S40 refers to the series of 5 samples with alternately grown BCT and BZT with a total of 40 layers, and S40C refers to the specific sample C in the S40 series. With increasing

total number of layers, the thickness of each interlayer is expected to reduce from \sim 12 unit-cells for S40*C* to \sim 2 unit-cells for S240*C*.

Structural characterization of BCT-BZT films

The as-grown BCT-BZT films are first measured at the Advanced Photon Source to characterize the film structure with a spatial resolution of a few tens of micrometers. The sample arrangement and X-ray scan direction is illustrated in Fig. S1. Fig. 1D displays the XRD intensities for S240. As shown, the STO and SRO peaks are constant, while the BCT-BZT (002) peaks exhibit a smooth shift from A to E, indicating a composition gradient. Fig. 1E shows the out-of-plane c-lattice parameters (d-spacing) for BCT-BZT, SRO, and STO as a function of location on the film. The clattice constant of S240 decreases from 4.05 Å at S240A (BZT phase dominant region) to 3.98 Å at S240E (BCT phase dominant region). This is consistent with the deposition setup that A is onaxis with the BZT target while E is on-axis with the BCT target. The lattice parameter difference can be explained by the cation radii relationship. Since $R_{Zr^{4+}}$ (0.72 Å) $> R_{Ti^{4+}}$ (0.605 Å) and $R_{Ca^{2+}}$ (1.00 Å) $\leq R_{Ba^{2+}}$ (1.35 Å), substituting Zr^{4+} for Ti^{4+} results in a larger lattice parameter in the BZT; in contrast, the substitution of Ba^{2+} by Ca^{2+} leads to a smaller lattice parameter for the BCT phase. The calculated d-spacing results from XRD are in good agreement with those previously reported for BCT-BZT films (9, 24, 25). It should be noted that the lattice parameter variation for the three samples in the middle (e.g., B, C and D) seems linear.

Figs. 1F and 1G show the XRD data and c-lattice parameters of the S40 series. The first and second order satellite peaks are clearly seen in S40, indicating the periodic SL structures. The d-spacing values calculated from the (002) peak positions show the same varying trend and almost identical values to those of S240. Based on the \pm 1st order satellite peak positions, the periodicity of the S40 SL is calculated to be ~9.5 nm at S40C, and it decreases toward the edges (A, E), reaching ~8.5

nm at S40*E* (Fig. S2). This thickness profile is typical for the cPLD method and has been reported previously (26-28). Similar XRD results are observed for the S80 series (Fig. S3) with a SL periodicity of ~4.7 nm at S80*C* and ~4.2 nm at S80*A* or S80*E*.

The microstructures of these films are further characterized via STEM. The low-magnification STEM images shown in Fig. 2A-C for the S40C, S80C and S240C BCT-BZT films reveal that the S40C and S80C films exhibit obvious SL structures, whereas the S240C film shows a single phase, indicating the intermixing of BCT and BZT phases, as reflected in the schematics of Fig. 1. Highangle annular dark-field (HAADF) STEM images (Fig. 2D-F) and energy-dispersive X-ray spectroscopy (EDS) maps of Ca and Zr (Fig. 2G-I) confirm the SL structures of the S40C and S80C films as well as the single-phase of S240C. Based on these HAADF-STEM images and EDS maps, the periodicity of the S40C and S80C SLs, i.e. BCT/BZT bilayer thickness, are estimated to be ~10.0 and ~5.0 nm, which are in good agreement with the calculated values from the XRD data (Fig. S2 and Fig. S3D). If S240C were to form a SL structure, the periodicity would have been close to ~ 1.7 nm, corresponding to 2 unit-cells of BZT and 2 unit-cells of BCT. However, the HAADF-STEM image shown in Fig. 2F exhibits the uniform single-phase structure for S240C without any visible phase or grain boundaries. Due to a fast growth rate of 0.6-0.7 Å/pulse for the on-axis growth (near samples A or E), the interdiffusion across different layers resulted in a solid solution for S240. Interdiffusion therefore provides a unique way to generate solid solution thin films with a composition gradient.

We also investigate the microstructures of S40 from A to E to confirm the composition and geometry gradient, as shown in Fig. S4. HAADF-STEM images and EDS elemental maps of Ca and Zr show a clear compositional variation from BZT dominant in S40A (~75% volume of BZT) to BCT dominant in S40E (~70% volume of BCT). Furthermore, geometric phase analysis (GPA)

was performed on the HAADF-STEM along the out-of-plane (ε_{yy}) and in-plane (ε_{xx}) directions to directly visualize lattice variations in the BCT-BZT SLs, as shown in Fig. S5. The reference regions are taken from the clean and undistorted BZT interlayer areas in all the HAADF-STEM images. The out-of-plane (ε_{yy}) strain maps show abrupt changes at the BCT and BZT interfaces due to their different intrinsic lattice constants, which result in tensile (positive) strain in BZT and compressive (negative) strain in BCT. Moreover, it is observed that S40*C* film (Fig. S5A) exhibits a homogeneous in-plane (ε_{xx}) strain map, while the ε_{xx} maps of S40*A* (Fig. S5B) and S40*E* (Fig. S5C) films show in-plane SL like structure, which might be related to some in-plane domain epitaxy structures formed during the film growth. The S80*C* film shows a typical BCT/BZT out-of-plane SL structure and in-plane SL like structure as well (Fig. S6A). More interestingly, the out-of-plane strain map of S240*A* also shows some SL like structures, but no SL structure was observed in the corresponding HAADF-STEM image (Fig. S6B). This can be ascribed to the extreme sensitivity of GPA strain analysis to atomic-scale lattice variations, while HAADF-STEM Z-contrast imaging is more sensitive to elemental character.

Ferroelectric and dielectric properties of BCT-BZT films

Next, ferroelectric properties of the BCT-BZT films are investigated. For simplicity, the results of S40 and S240 films are shown in Figure 3 for direct comparison. Fig. 3A and 3B show ferroelectric polarization (P) maps of the S40 and S240 films measured under 700 kV/cm electric field at three different frequencies of 1 kHz, 10 kHz, and 100 kHz. Six polarization datapoints were measured at each sample (see Fig. S1) along the composition gradient direction. Thus, there are 90 datapoints shown in each polarization map. The polarization values of both series are found to exhibit similar trends with the highest P values obtained near sample D (yellow shaded area). At an electric field of 700 kV/cm, the highest P values for S40D and S240D are estimated by Lorentzian fitting to the

data to be ~18 μ C/cm² and ~22 μ C/cm², respectively. Figure 3C and 3D show the energy storage density (W) and energy storage efficiency (η) of S40 and S240 films calculated based on their measured polarization vs. electric field (P-E) hysteresis loops. For both S40 and S240, W first increases to a maximum near sample D and then decreases. The η values for S40 follow the same trend, reaching a maximum value of ~80 % at S40D. The η values for S240 are location independent (~80-91% from A to E), with the maximum η (91%) higher than the current state-of-the-art in PZT, BTO-BFO-STO, and BZT-BCT systems (12, 29, 30). In sum, W and η reach their maximum values near sample D location. In addition, the electric field and frequency dependent data for S40 and S240 films (Fig. S8) demonstrate that the energy storage density W is noticeably impacted by the magnitude and frequency of the applied electric fields, while energy storage efficiency η values in general are much more stable across different measurement parameters.

Piezoresponse force microscopy (PFM) was used to confirm the ferroelectricity and obtain the piezoelectric coefficient (d_{33}) values of the samples. More detailed information can be found in Fig. S9 and Supplementary Materials. The d_{33} values of S40 and S240 are summarized in Figure 3E. Both series show the highest d_{33} values near sample D, and the minor left-shift of the maximum values compared to those in the polarization maps (Figs. 3A and B) may be attributed to coarser sampling in the PFM measurements. It is also noted that the d_{33} values of S240 films are, in general, much higher than those of S40 films. This indicates that the mixed solid solution phase of BZT-BCT films have higher d_{33} values than BZT/BCT SL films, which is consistent with previous reports (31-33). Figure 3F depicts the schematic illustration of the PFM experiment setup and the "Los Alamos National Laboratory" logo written on the S240D film surface (close to the highest d_{33} point at D) by controlling the local ferroelectric domains via electrical polarization. The clear piezoresponse amplitude contrast between the polarized and unpolarized regions confirms the

ferroelectric response of the film. Furthermore, based on the P-E hysteresis loops of both S40D and S240D (Fig. S10), the S240 film (Fig. S10C) exhibits smaller coercivity than the S40 film. The slim P-E loops, small remnant polarizations and coercivity fields indicate a possible relaxor ferroelectric behavior for S240. This is consistent with our recent work on the growth of BZT-BCT solid solution films that show relaxor ferroelectric behavior in this system (30, 34). The coercive fields (H_c) of both films at samples C and D are further extracted and plotted in Fig. S11, showing that the lowest H_c of both films are obtained near sample D. Furthermore, fatigue and retention measurements (Fig. S12) show that both films exhibit near zero reduction of the remanent polarization for over 10^9 cycles or 24 hours after the experiment was terminated, indicating a strong stability of the remanent polarization against cycling fatigue and retention time.

The dielectric properties of the S40 and S240 BCT-BZT films were obtained from the measured capacitance vs. voltage (C-V) curves. The permittivity values are found to follow the same location-dependent trend as polarization (Figs. 3A, B) and energy storage density (Figs. 3C, D). Namely, as shown in Figs. 3G and 3H, the dielectric permittivity (ε_r) of both series exhibit the highest ε_r values at sample D, increasing from ~130 at sample A to ~300 at sample D in S40 and from ~320 at A to ~680 at D in S240. Overall, S240 exhibits higher permittivity and polarization across samples than S40. The insets in Fig 3G and 3H show typical butterfly shaped C-V curves at sample D, demonstrating the ferroelectric nature of these films. The measured dielectric losses (tan δ) of both films show limited location-dependence and are less than 0.5, indicating the stable dielectric properties for both series. Fig. 3I summarizes the dielectric tunability and loss tangent of both films at different sample locations. It is noted that S240 maintains a high dielectric tunability of 60~70% while S40 has lower tunability values of 35~45 %. More interestingly, the dielectric tunability is insensitive to location and is, therefore, likely controlled by film geometry

(SL or single phase) rather than composition. Hence, in terms of properties including polarization, piezoelectric coefficient, permittivity, and dielectric tunability, the mixed solid solution BZT-BCT films (S240) are superior to SL films (S40).

Property tuning mechanism of BCT-BZT films

It is well known that for ferroelectric material the high piezoelectricity stems from its morphotropic phase boundary (MPB), where the free energy is isotropic with very low energy barrier for polarization rotation and lattice distortion (10). Previous works show that the highest piezoelectric and dielectric properties are obtained at 50BZT-50BCT bulk ceramics (10, 13). Based on our measurements, the best ferroelectric and dielectric properties of the BCT-BZT thin films are present near sample D. Therefore, it is essential to investigate the microstructure and identify the BCT: BZT phase ratio for the SL and solid solution films at their "optimal property points". To obtain this critical information, we performed high-resolution analytical STEM, including imaging, EDS mapping and elemental quantification, and electron energy-loss spectroscopy (EELS) for the S40D and S240D at their "optimal property locations". Figs. 4A-C show the HAADF-STEM image and corresponding out-of-plane (ε_{yy}) and in-plane (ε_{xx}) strain maps of S40D film. It is interesting to note that the ε_{yy} strain map shows somewhat curved layer interface in contrast to the pretty straight BCT/BZT interface observed in the HAADF image. This indicates the strain field within the SL structure is more sensitive to the local defects or grain boundaries which are not visible in the Z-contrast HAADF image. The ε_{xx} map shows the in-plane inhomogeneity of the SL film. The composite EDS elemental map for Ca and Zr (Fig. 4D), along with their intensity line profiles (Fig. 4E and Fig. S13), reveal the typical (BCT/BZT)_N SL structure with each layer being ~5 nm thick. The distinct BCT/BZT interface indicates the limited interdiffusion during film growth. EDS elemental quantification for S40D is shown in Table S1,

where the Ca/Zr atomic ratio is ~ 1.07 . Meanwhile, the EDS elemental maps of the S240*D* solid-solution film are shown in Fig. S14. EDS elemental quantification results for S240*D* are shown in Table S2, and the Ca/Zr atomic ratio is ~ 1.10 . Therefore, for both the S40 and the S240 film series, the "optimal property" is achieved for BCT: BZT ≈ 1.07 -1.10, corresponding to a chemical composition of 48BZT-52BCT. The minor difference between our MPB composition (48BZT-52BCT) and the reported MPB composition in the bulk BCT-BZT ceramics (50BZT-50BCT) can be attributed to the fact that thin films are often subjected to lattice strains, oxygen vacancies and other defects which are not present in bulk materials, which may lead to a shift of the triple point in the BCT-BZT phase diagram.

The above results show that the SL periodicity plays a critical role in impacting the ferroelectric and dielectric properties. Although the S240 series exhibits enhanced ferroelectric properties relative to the S40 series, S240 exhibits higher dielectric leakage (Fig. 3I). The dielectric loss in ferroelectrics is found to be closely related to defects chemistry and charge-trapping phenomena within the studied materials, where oxygen vacancies play an important role in these processes (35-37). Hence, it is necessary to investigate the oxygen vacancies concentration (V_0) and valence states of transitional metals for the BCT-BZT films near its MPB composition. We therefore conducted EELS experiments for S40D and S240D, as summarized in Fig. 5. Figs. 5A and 5B display EELS O-K energy-loss near-edge structure (ELNES) extracted from different locations within the S40D SL and S240D solid-solution films and STO substrate (for reference), respectively. Several fine-structure features are present and labeled "A", "B", "C", and "D". The pre-peak "A" represents transitions from the O 1s to unoccupied O 2p hybridized with Ti 3d band states (3s-40). Both S40D and S240D films show decreased pre-peak intensities compared to that of the STO substrates, indicating the decreased number of unoccupied states in Ti 3d band for the

BCT-BZT films. This can be explained by the valence change of Ti from Ti⁴⁺ to Ti³⁺, namely doping one electron per site into the empty Ti 3d band $(3d^0$ to $3d^1$) to make the excitation of these states less likely, leading to a decrease in the pre-peak intensities. The "B", "C", and "D" peaks are mainly originated from the transition hybridized states between O 2p and A-site cation (*i.e.* Sr 4d and Ba 5d) bands, Ti 4s and 4p bands, respectively (38,41-43). It is noted that the "C" peak in both films splits into two subpeaks and are labeled as "C₁" and "C₂". This can be explained by the fact that displaced Ti atoms in the BTO octahedra that leads to polarization breaks the symmetry of oxygen atoms and causes the energy splitting (39). Overall, the O K-edges of both BCT-BZT films exhibit damped intensities for all peaks, which can be explained by the presence of oxygen vacancies in the studied materials (38,44-46).

To further investigate the oxidation (valence) states of Ti, we collected EELS spectra of the Ti $L_{2,3}$ edges for the S40D and S240D films, as plotted in Fig. 5C and 5D. In comparison to the STO reference, the peak positions of the $L_{2,3}$ edges of both films undergo minor shifts to lower energy loss values, indicating the reduction of the Ti oxidation state (46-48). The L_3/L_2 intensity ratio can be correlated with the oxidation states of middle or late 3d transition metals (TM) (47-50). However, for early 3d TM such as Ti, this method is difficult to apply due to the overlapping of the L_2 and L_3 edges. Stoyanov *et al.* and Shao *et al.* have proposed to calculate Ti $L_{2,3}$ intensity ratio by using a reduced energy window to estimate the Ti valence and Ti⁴⁺/Ti³⁺ fractions for a series of Ti oxides (48,51). Here, an energy window of lev is used to calculate the Ti L_3/L_2 intensity ratio based on the raw Ti- $L_{2,3}$ ELNES spectra (Fig. 5C and 5D). Figs. 5E and 5F summarize the calculated Ti $L_{2,3}$ ratios extracted from different locations on the S40D and S240D films. The uncertainty comes from multiple spectrum collections for the single data column. It is shown that the Ti $L_{2,3}$ ratio in STO substrate is ~ 0.75. For the S40D SL, the L_3/L_2 ratios in the BZT or BCT

phase regions increase to slightly higher than 0.77, whereas at the BZT/BCT interface it is \sim 0.79; For the S240D solid solution, the L_3/L_2 ratio is higher at 0.79 and increases to 0.80 near the surface of the film. The multiple spectrum collections in the same area show consistent results with the standard deviation less than 0.005, which minimizes the uncertainty and noise level for the calculated result. As TM oxidation states decrease as the L_3/L_2 ratio increases (47-51), together with the more noticeable $L_{2,3}$ peak shifts shown in the S240D, we can conclude that the average Ti valence state of the S240D film is lower than that of the S40D SL film, indicating a higher V_O concentration in the solid-solution film than in the SL film. This finding can also explain the higher dielectric loss of the S240D film (Fig. 3I), which further confirms that oxygen vacancies are a key factor impacting dielectric properties. The Ba- $M_{4,5}$ edges of both films show no peak shift (Fig. S15), and no $M_{4,5}$ intensity changes are detected, indicating that the valence states of Ba atoms (A-site) are much less sensitive to the oxygen stoichiometry than the valence states of Ti (B-site) for the perovskite structure (ABO_{3-6}) oxides.

Recently, polar displacement vector maps based on atomic-resolution STEM imaging has been demonstrated as an effective method for visualizing the polarization fields and domain structures of ferroelectric materials (52-55). In this work, based on the aberration-corrected Z-contrast HAADF-STEM images, we generate the polarization displacement vector maps along the <100> projection axis for the S40, S80, and S240 films near its MPB composition by using the TopoTEM code package (56) (see Supplementary Materials for details). As shown in Figure 6, the projected polarization vector of each Ti atom (δ_{Ti}) is overlaid on the original aberration-corrected ADF-STEM image, and the color of the δ_{Ti} vector is determined by its polarization direction. Hence, from this displacement vector map we can identify the differently oriented polar nano domains (PND) by the color of the vectors. Figs. 6B and 6C show the displacement vector maps of the

S40*D* and S240*D* films, respectively. The corresponding raw HAADF-STEM images are shown in Fig. S16A and S16B. The yellow dashed lines in Fig. 6B indicate the BCT/BZT interfaces of the SL film. The majority of Fig. 6B shows uniform polar vector directions, while differently oriented polar domains (shown in dashed colored circles) are present mainly near the BCT/BZT interface. In contrast, the vector map of the S240D solid solution film (Fig. 6C) exhibits many randomly oriented PND with averagely smaller sizes. The STEM image and corresponding displacement vector map of the S80C film (Fig. S16C and D) show a higher number of differently oriented PND than the S40 SL (Fig. 6B) with most of which are at the BCT/BZT interfaces. In summary, the polarization displacement maps of $\{BCT-BZT\}_N$ (N = 40, 80, 240) films reveal that the PND sizes and distributions within ferroelectric thin films can be artificially controlled via tuning the thickness and spacing of polar layers. The decrease of ferroelectric interlayer thickness leads to smaller size and random orientations of PND and promotes the transition from regular ferroelectric-like SL to relaxor-like behavior of the solid solutions.

Conclusions

We have demonstrated a high-throughput combinatorial pulsed laser deposition (cPLD) technique to grow epitaxial ferroelectric BCT-BZT films with superlattice structure and mixed solid solution phase. A compositional gradient is achieved across a 1-inch film area. By controlling the thickness of each SL layer from several nanometers down to 2 unit cells, the film microstructure transitions from a distinct SL to single-phase solid solution, with an associated change from ferroelectric-like to relaxor-like behavior due to the tuning of polar nano domain (PND) size. Location-dependent ferroelectric and dielectric property maps enable selection of the "optimal property point" of the

nanocomposite and identify its morphotropic phase boundary (MPB) composition point from a single specimen. This high-throughput combinatorial synthesis approach can be applied to many materials systems to significantly expedite the property optimization process.

References and Notes

- 1. V. V Shvartsman, D. C. Lupascu, Lead-free relaxor ferroelectrics. *J. Am. Ceram. Soc.*. **95**, 1–26 (2012).
- 2. P. K. Panda, Environmental friendly lead-free piezoelectric materials. *J. Mater. Sci.* **44**, 5049–5062 (2009).
- 3. L. Yang, X. Kong, F. Li, H. Hao, Z. Cheng, H. Liu, J.-F. Li, S. Zhang, Perovskite lead-free dielectrics for energy storage applications. *Prog. Mater. Sci.* **102**, 72–108 (2019).
- 4. M. Acosta, N. Novak, V. Rojas, S. Patel, R. Vaish, J. Koruza, G. A. Rossetti, J. Rödel, BaTiO₃-based piezoelectrics: Fundamentals, current status, and perspectives. *Appl. Phys. Rev.* **4** (2017).
- 5. Y. Tsur, T. D. Dunbar, C. A. Randall, Crystal and defect chemistry of rare earth cations in BaTiO₃. *J. Electroceram.* 7, 25–34 (2001).
- 6. Y. Li, W. Chen, J. Zhou, Q. Xu, H. Sun, R. Xu, Dielectric and piezoelectric properties of lead-free (Na_{0.5}Bi_{0.5})TiO₃–NaNbO₃ ceramics. *Mater. Sci. Eng. B.* **112**, 5–9 (2004).
- 7. H.-J. Ye, X.-S. Qian, D.-Y. Jeong, S. Zhang, Y. Zhou, W.-Z. Shao, L. Zhen, Q. M. Zhang, Giant electrocaloric effect in BaZr_{0.2}Ti_{0.8}O₃ thick film. *Appl. Phys. Lett.* **105**, 152908 (2014).
- 8. W.-B. Li, D. Zhou, L.-X. Pang, Enhanced energy storage density by inducing defect dipoles in lead free relaxor ferroelectric BaTiO₃-based ceramics. *Appl. Phys. Lett.* **110**, 132902 (2017).
- 9. Z. Liu, R. Yuan, D. Xue, W. Cao, T. Lookman, Origin of large electrostrain in Sn^{4+} doped $Ba(Zr_{0.2}Ti_{0.8})O_{3-x}(Ba_{0.7}Ca_{0.3})TiO_3$ ceramics. *Acta Mater.* **157**, 155–164 (2018).
- 10. W. Liu, X. Ren, Large piezoelectric effect in Pb-free ceramics. *Phys. Rev. Lett.* **103**, 257602 (2009).
- 11. T. Mikolajick, M.-H. Park, L. Begon-Lours, S. Slesazeck, From ferroelectric material optimization to neuromorphic devices. *Adv. Mater.* **35**, 2206042 (2023).
- 12. H. Pan, F. Li, Y. Liu, Q. Zhang, M. Wang, S. Lan, Y. Zheng, J. Ma, L. Gu, Y. Shen, Ultrahigh–energy density lead-free dielectric films via polymorphic nanodomain design. *Science* **365**, 578–582 (2019).
- 13. D. Xue, Y. Zhou, H. Bao, C. Zhou, J. Gao, X. Ren, Elastic, piezoelectric, and dielectric properties of Ba(Zr_{0.2}Ti_{0.8})O₃-50(Ba_{0.7}Ca_{0.3})TiO₃ Pb-free ceramic at the morphotropic phase boundary. *J. Appl Phys.* **109**, 054110 (2011).

- 14. W. Chen, X. Zhao, J. Sun, L. Zhang, L. Zhong, Effect of the Mn doping concentration on the dielectric and ferroelectric properties of different-routes-fabricated BaTiO₃-based ceramics. *J. Alloys Compd.* **670**, 48–54 (2016).
- 15. Y. Huang, C. Zhao, S. Zhong, J. Wu, Highly tunable multifunctional BaTiO₃-based ferroelectrics via site selective doping strategy. *Acta Mater.* **209**, 116792 (2021).
- 16. A. Chen, Q. Su, H. Han, E. Enriquez, Q. Jia, Metal oxide nanocomposites: a perspective from strain, defect, and interface. *Adv. Mater.* **31**, 1803241 (2019).
- 17. X.-D. Xiang, X. Sun, G. Briceno, Y. Lou, K.-A. Wang, H. Chang, W. G. Wallace-Freedman, S.-W. Chen, P. G. Schultz, A combinatorial approach to materials discovery. *Science*. **268**, 1738–1740 (1995).
- 18. H. Koinuma, I. Takeuchi, Combinatorial solid-state chemistry of inorganic materials. *Nat. Mater.* **3**, 429–438 (2004).
- 19. A. Ludwig, Discovery of new materials using combinatorial synthesis and high-throughput characterization of thin-film materials libraries combined with computational methods. *NPJ Comput Mater.* **5**, 70 (2019).
- 20. S. Curtarolo, G. L. W. Hart, M. B. Nardelli, N. Mingo, S. Sanvito, O. Levy, The high-throughput highway to computational materials design. *Nat. Mater.* **12**, 191–201 (2013).
- 21. J. Cui, Y. S. Chu, O. O. Famodu, Y. Furuya, J. Hattrick-Simpers, R. D. James, A. Ludwig, S. Thienhaus, M. Wuttig, Z. Zhang, Combinatorial search of thermoelastic shape-memory alloys with extremely small hysteresis width. *Nat. Mater.* **5**, 286–290 (2006).
- 22. M. L. Green, I. Takeuchi, J. R. Hattrick-Simpers, Applications of high throughput (combinatorial) methodologies to electronic, magnetic, optical, and energy-related materials. *J. Appl. Phys.* **113**, 231101 (2013).
- 23. M. Zeng, Y. Du, Q. Jiang, N. Kempf, C. Wei, M. V Bimrose, A. N. M. Tanvir, H. Xu, J. Chen, D. J. Kirsch, High-throughput printing of combinatorial materials from aerosols. *Nature*. **617**, 292–298 (2023).
- 24. A. Bjørnetun Haugen, J. S. Forrester, D. Damjanovic, B. Li, K. J. Bowman, J. L. Jones, Structure and phase transitions in 0.5(Ba_{0.7}Ca_{0.3}TiO₃)-0.5(BaZr_{0.2}Ti_{0.8}O₃) from -100° C to 150° C. *J. Appl. Phys.* **113**, 014103 (2013).
- 25. N. D. Scarisoreanu, F. Craciun, A. Moldovan, V. Ion, R. Birjega, C. Ghica, R. F. Negrea, M. Dinescu, High permittivity (1–x) Ba(Zr_{0.2}Ti_{0.8})O₃ x(Ba_{0.7}Ca_{0.3})TiO₃ (x= 0.45) epitaxial thin films with nanoscale phase fluctuations. *ACS Appl Mater Interfaces*. 7, 23984–23992 (2015).
- 26. H.-T. Zhang, L. Zhang, D. Mukherjee, Y.-X. Zheng, R. C. Haislmaier, N. Alem, R. Engel-Herbert, Wafer-scale growth of VO2 thin films using a combinatorial approach. *Nat. Commun.* **6**, 8475 (2015).
- 27. M. Lippmaa, T. Koida, H. Minami, Z. W. Jin, M. Kawasaki, H. Koinuma, Design of compact pulsed laser deposition chambers for the growth of combinatorial oxide thin film libraries. *Appl. Surf. Sci.* **189**, 205–209 (2002).
- 28. H. Lysne, T. Brakstad, M. Kildemo, T. Reenaas, Improved methods for design of PLD and combinatorial PLD films. *J. Appl. Phys.* **132**, 125301 (2022).

- 29. F. Li, M. J. Cabral, B. Xu, Z. Cheng, E. C. Dickey, J. M. LeBeau, J. Wang, J. Luo, S. Taylor, W. Hackenberger, Giant piezoelectricity of Sm-doped Pb (Mg1/3Nb2/3) O3-PbTiO3 single crystals. *Science* **364**, 264–268 (2019).
- 30. R. Yuan, A. Kumar, S. Zhuang, N. Cucciniello, T. Lu, D. Xue, A. Penn, A. R. Mazza, Q. Jia, Y. Liu, Machine Learning-Enabled Superior Energy Storage in Ferroelectric Films with a Slush-Like Polar State. *Nano. Lett.* **23**, 4807 (2023).
- 31. Z. Sun, C. Ma, M. Liu, J. Cui, L. Lu, J. Lu, X. Lou, L. Jin, H. Wang, C. Jia, Ultrahigh energy storage performance of lead-free oxide multilayer film capacitors via interface engineering. *Adv. Mater.* **29**, 1604427 (2017).
- 32. Q. Fan, M. Liu, C. Ma, L. Wang, S. Ren, L. Lu, X. Lou, C.-L. Jia, Significantly enhanced energy storage density with superior thermal stability by optimizing Ba(Zr_{0.15}Ti_{0.85})O₃/Ba(Zr_{0.35}Ti_{0.65})O₃ multilayer structure. *Nano Energy.* **51**, 539–545 (2018).
- 33. A. P. Sharma, D. K. Pradhan, S. K. Pradhan, M. Bahoura, Large energy storage density performance of epitaxial BCT/BZT heterostructures via interface engineering. *Sci. Rep.* **9**, 16809 (2019).
- 34. N. Cucciniello, A.-R. Mazza, P. Roy, S. Kunwar, D. Zhang, H.-Y. Feng, K. Arsky, A. Chen, Q. Jia, Anisotropic Properties of Epitaxial Ferroelectric Lead-Free 0.5[Ba(Ti_{0.8}Zr_{0.2})O₃]-0.5(Ba_{0.7}Ca_{0.3})TiO₃ Films. *Materials.* **16**, 6671 (2023).
- 35. K. H. Härdtl, Electrical and mechanical losses in ferroelectric ceramics. *Ceram. Int.* **8**, 121–127 (1982).
- 36. W. L. Warren, D. Dimos, R. M. Waser, Degradation mechanisms in ferroelectric and high-permittivity perovskites. *MRS Bull.* **21**, 40–45 (1996).
- 37. A. Chen, W. Zhang, L. R. Dedon, D. Chen, F. Khatkhatay, J. L. MacManus-Driscoll, H. Wang, D. Yarotski, J. Chen, X. Gao, Couplings of polarization with interfacial deep trap and Schottky interface controlled ferroelectric memristive switching. *Adv. Funct. Mater.* **30**, 2000664 (2020).
- 38. L. F. Kourkoutis, H. L. Xin, T. Higuchi, Y. Hotta, J. H. Lee, Y. Hikita, D. G. Schlom, H. Y. Hwang, D. A. Muller, Atomic-resolution spectroscopic imaging of oxide interfaces. *Phil. Mag.* **90**, 4731–4749 (2010).
- 39. G. Liu, Y. Wang, B. Zou, W. Liang, N. M. Alford, D. W. McComb, P. K. Petrov, Probing the Electronic Structures of BaTiO₃/SrTiO₃ Multilayered Film with Spatially Resolved Electron Energy-Loss Spectroscopy. *J. Phys. Chem. C* **120**, 16681–16686 (2016).
- 40. Z. Zhang, W. Sigle, M. Rühle, Atomic and electronic characterization of the a [100] dislocation core in SrTiO₃. *Phys. Rev. B* **66**, 094108 (2002).
- 41. A. Torres-Pardo, A. Gloter, P. Zubko, N. Jecklin, C. Lichtensteiger, C. Colliex, J.-M. Triscone, O. Stéphan, Spectroscopic mapping of local structural distortions in ferroelectric PbTiO₃/SrTiO₃ superlattices at the unit-cell scale. *Phys. Rev. B* **84**, 220102 (2011).
- 42. H. Kurata, S. Isojima, M. Kawai, Y. Shimakawa, S. Isoda, Local analysis of the edge dislocation core in BaTiO₃ thin film by STEM-EELS. *J Microsc.* **236**, 128–131 (2009).
- 43. M. Abbate, J. C. Fuggle, A. Fujimori, L. H. Tjeng, C. T. Chen, R. Potze, G. A. Sawatzky, H. Eisaki, S. Uchida, Electronic structure and spin-state transition of LaCoO₃. *Phys. Rev. B.* **47**, 16124 (1993).

- 44. D. A. Muller, N. Nakagawa, A. Ohtomo, J. L. Grazul, H. Y. Hwang, Atomic-scale imaging of nanoengineered oxygen vacancy profiles in SrTiO₃. *Nature* **430**, 657–661 (2004).
- 45. R. F. Klie, N. D. Browning, Atomic scale characterization of oxygen vacancy segregation at SrTiO₃ grain boundaries. *MRS Online Proceedings Library* **654**, 171–176 (2000).
- 46. H. K. Schmid, W. Mader, Oxidation states of Mn and Fe in various compound oxide systems. *Micron* **37**, 426–432 (2006).
- 47. H. Tan, J. Verbeeck, A. Abakumov, G. V. Tendeloo, Oxidation state and chemical shift investigation in transition metal oxides by EELS. *Ultramicroscopy* **116**, 24-33 (2012).
- 48. Y. Shao, C. Maunders, D. Rossouw, T. Kolodiazhnyi, G. A. Botton, Quantification of the Ti oxidation state in BaTi_{1-x}Nb_xO₃ compounds. *Ultramicroscopy* **110**, 1014-1019 (2010).
- 49. M. Varela, M. P. Oxley, W. Luo, J. Tao, M. Watanabe, A. R. Lupini, S. T. Pantelides, S. J. Pennycook, Atomic-resolution imaging of oxidation states in manganites. *Phys. Rev. B* **79**, 085117 (2009).
- 50. D. Li, H. Wang, K. Li, B. Zhu, K. Jiang, D. Backes, L. S. I. Veiga, J. Shi, P. Roy, M. Xiao, Emergent and robust ferromagnetic-insulating state in highly strained ferroelastic LaCoO₃ thin films. *Nat. Commun.* **14**, 3638 (2023).
- 51. E. Stoyanov, F. Langenhorst, G. Steinle-Neumann, The effect of valence state and site geometry on Ti $L_{3,2}$ and O K electron energy-loss spectra of Ti_xO_y phases. *Am. Mineral.* **92**, 577–586 (2007).
- 52. C. T. Nelson, B. Winchester, Y. Zhang, S.-J. Kim, A. Melville, C. Adamo, C. M. Folkman, S.-H. Baek, C.-B. Eom, D. G. Schlom, Spontaneous vortex nanodomain arrays at ferroelectric heterointerfaces. *Nano. Lett.* **11**, 828–834 (2011).
- 53. Y. L. Tang, Y. L. Zhu, X. L. Ma, A. Y. Borisevich, A. N. Morozovska, E. A. Eliseev, W. Y. Wang, Y. J. Wang, Y. B. Xu, Z. D. Zhang, Observation of a periodic array of flux-closure quadrants in strained ferroelectric PbTiO₃ films. *Science* **348**, 547–551 (2015).
- 54. A. K. Yadav, C. T. Nelson, S. L. Hsu, Z. Hong, J. D. Clarkson, C. M. Schlepütz, A. R. Damodaran, P. Shafer, E. Arenholz, L. R. Dedon, Observation of polar vortices in oxide superlattices. *Nature*. **530**, 198–201 (2016).
- 55. A. Kumar, J. N. Baker, P. C. Bowes, M. J. Cabral, S. Zhang, E. C. Dickey, D. L. Irving, J. M. LeBeau, Atomic-resolution electron microscopy of nanoscale local structure in lead-based relaxor ferroelectrics. *Nat. Mater.* **20**, 62–67 (2021).
- 56. E. N. O'Connell, K. Moore, E. McFall, M. Hennessy, E. Moynihan, U. Bangert, M. Conroy, TopoTEM: A python package for quantifying and visualizing scanning transmission electron microscopy data of polar topologies. *Microsc. Microanal.* **28**, 1444–1452 (2022).

Acknowledgements

Funding: The work at Los Alamos National Laboratory was supported by the NNSA's Laboratory Directed Research and Development Program, and was performed, in part, at the Center for Integrated Nanotechnologies, an Office of Science User Facility operated for the U.S. Department of Energy (DOE) Office of Science by Los Alamos National Laboratory (contract 89233218NCA000001) and Sandia National Laboratories (contract DE-NA0003525). Alamos National Laboratory, an affirmative action equal opportunity employer, is managed by Triad National Security, LLC for the U.S. Department of Energy's NNSA, under Contract No. 89233218CNA000001. Sandia National Laboratories is a multiprogram laboratory managed and operated by National Technology and Engineering Solutions of Sandia, LLC, a wholly owned subsidiary of Honeywell International, Inc., for the U.S. Department of Energy's National Nuclear Security Administration under contract DE-NA0003525. This paper describes objective technical results and analysis. Any subjective views or opinions that might be expressed in the paper do not necessarily represent the views of the U.S. Department of Energy or the United States Government. The X-ray diffraction measurement at the Argonne National Laboratory was supported by the U.S. Department of Energy, Office of Science, Basic Energy Sciences, Materials Science and Engineering Division, and the XRD data analysis was based on work supported by Laboratory Directed Research and Development funding from Argonne National Laboratory, provided by the Director, Office of Science, of the U.S. Department of Energy and by the U.S. DOE Office of Science-Basic Energy Sciences under Contract No. DE-AC02-06CH11357. This research used resources of the Advanced Photon Source, a U.S. Department of Energy (DOE) Office of Science user facility operated for the DOE Office of Science by Argonne National Laboratory under Contract No. DE-AC02-06CH11357. The aberration-corrected HAADF-STEM portion of this research was supported by the Center for Nanophase Materials Sciences (CNMS), which is a US Department of Energy, Office of Science User Facility at Oak Ridge National Laboratory. The PFM measurements at Texas A&M University were supported by the National Science Foundation under the Award No. CMMI-2311573 and the donors of the ACS Petroleum Research Fund under Doctoral New Investigator Grant 62603-DNI10. Q.T. served as Principal Investigator on ACS 62603-DNI10 that provided support for D.K.

Author contributions

Competing interests: The authors declare no conflict of interest.

Data and materials availability

Supplementary Materials

Materials and Methods

Fig. S1-S16

References (57-62)

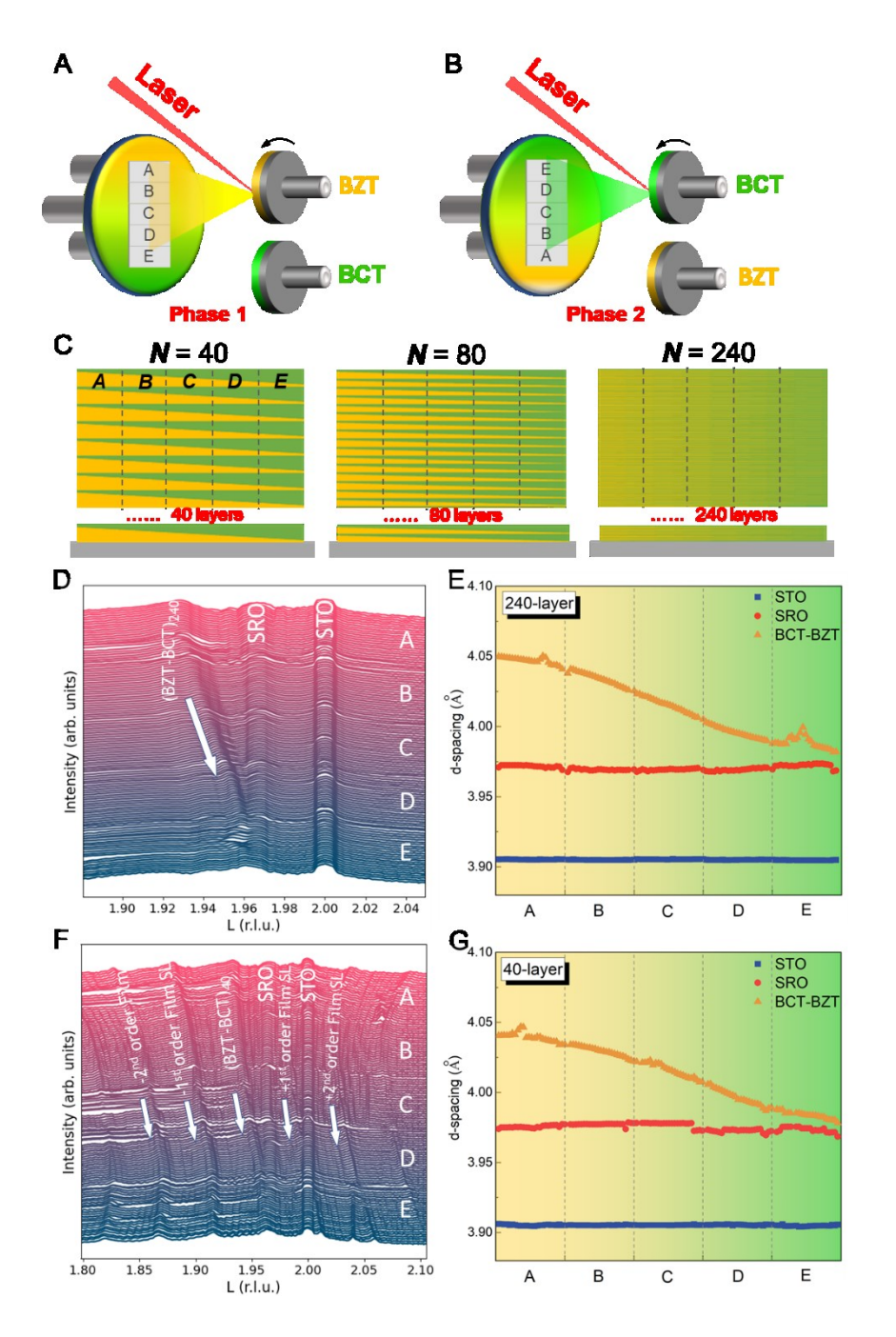


Fig. 1 Combinatorial synthesis and XRD patterns of $x(Ba_{0.7}Ca_{0.3})TiO_3 - (1-x)Ba(Zr_{0.2}Ti_{0.8})O_3$ (xBCT-(1-x)BZT) thin films. (A, B) Schematics of the combinatorial synthesis approach of growing the BCT-BZT thin films for Phase 1 and 2. (C) Schematics of the cross-sectional views of S40, S80, and S240 BCT-BZT films. XRD intensities and calculated c-lattice parameters (d-spacings) of (D, E) S240 and (F, G) S40 BCT-BZT films. The data were extracted from (002) reciprocal space maps. The film d-spacings as a function of position along the sample were evaluated from the peak L positions assuming Gaussian intensity distributions. r.l.u. = reciprocal lattice units. Note: the fringe patterns between two superlattice peaks are not real film thickness fringes but some artifacts due to the data processing of 3DRSM profiles.

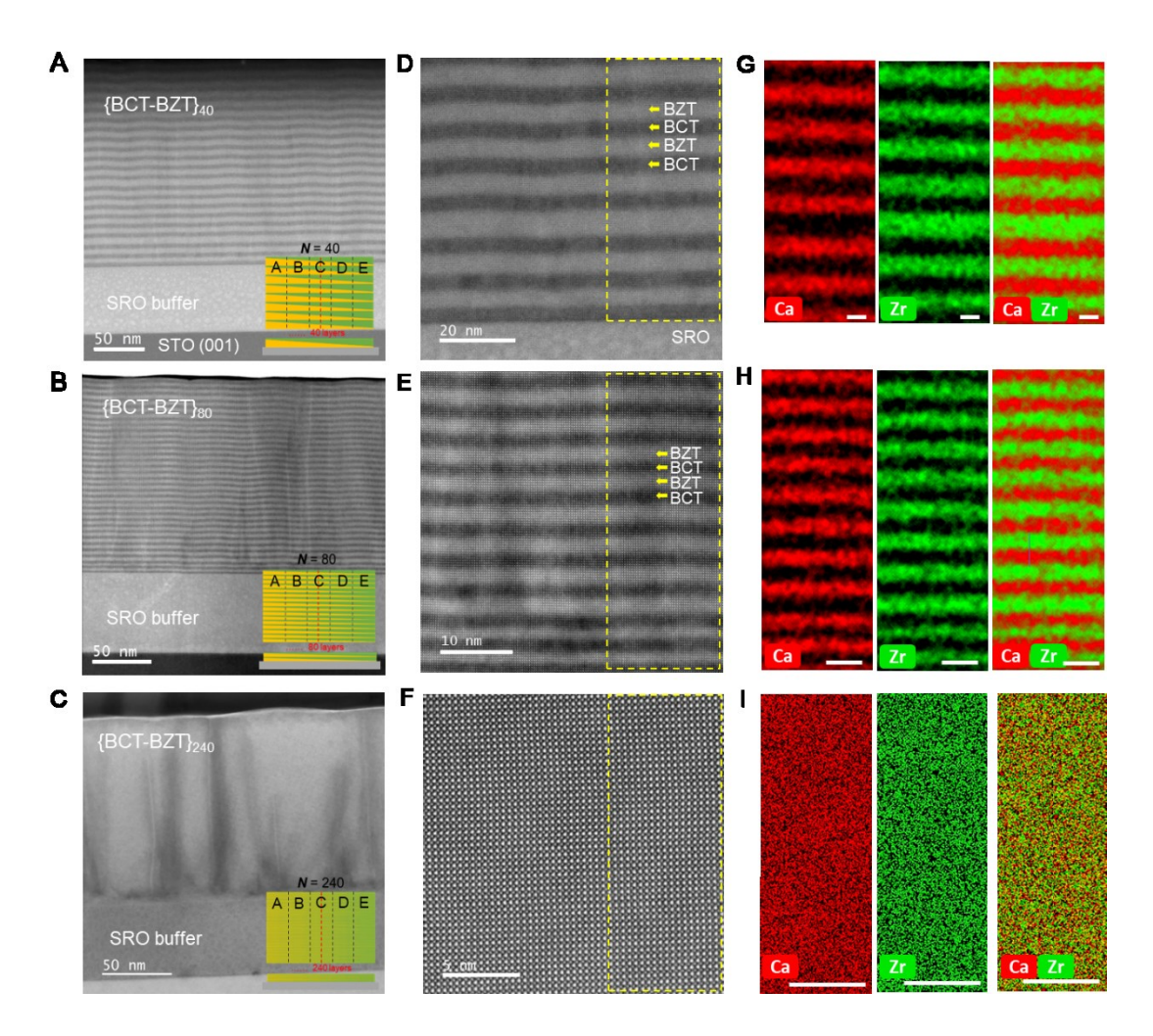


Fig. 2 Microstructural characterization of BCT-BZT films. (**A, B, C**) Low-magnification HAADF-STEM images of S40, S80, and S240 BCT-BZT thin films at center of location *C*. Insets are the schematics of the cross-sectional views of S40, S80, and S240 BCT-BZT films with the red dashed lines showing the investigated sample locations. (**D, E, F**) Atomic-resolution HAADF-STEM images of S40, S80, and S240 BCT-BZT thin films, where yellow dashed rectangles indicate areas of EDS maps. (**G, H, I**) Energy-dispersive X-ray spectroscopy (EDS) maps of Ca and Zr in S40, S80, and S240 BCT-BZT films. Scale bars in G, H, I: 5 nm.

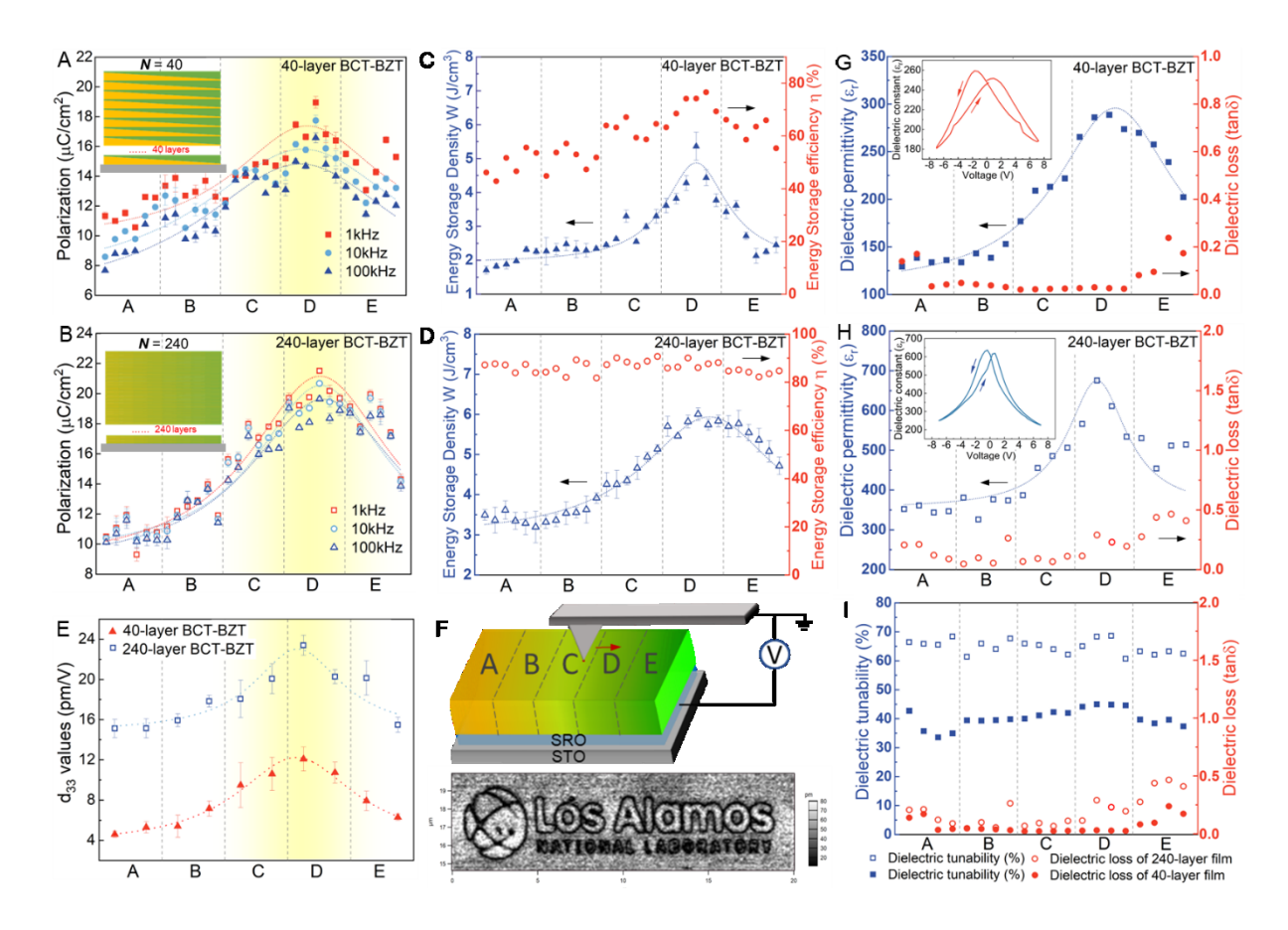


Fig. 3 Ferroelectric and dielectric properties of the *x*BCT-(1-*x*)BZT thin films. The location-dependent (**A**, **B**) ferroelectric polarization (*P*), (**C**, **D**) energy storage density (*W*) and efficiency (η), (**E**) piezoelectric coefficient (d_{33}), (**G**, **H**) dielectric permittivity (ε_r) and dielectric loss (tanδ), and (**I**) dielectric tunability (%) of S40 and S240 BCT-BZT thin films. (**F**) Schematic of the piezoelectric force microscopy (PFM) measurement and the vertical PFM amplitude map showing the "Los Alamos National Laboratory" logo. Insets are the schematic cross-sectional views of (A) S40 and (B) S240 BCT-BZT films; measured capacitance *vs.* voltage (*C-V*) curves of (G) S40 and (H) S240 BCT-BZT films.

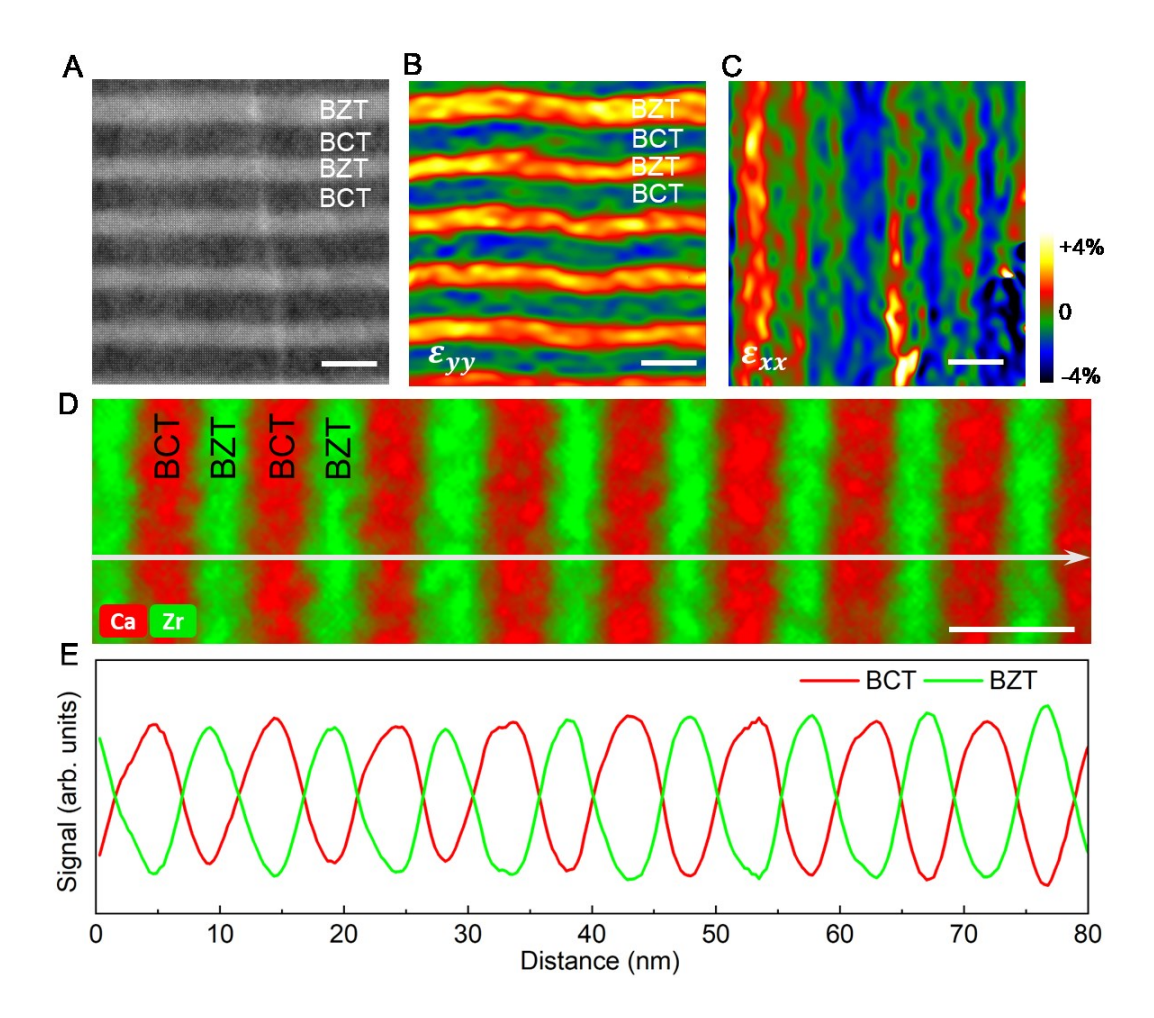


Fig. 4 Microstructure analysis of S40*D* BCT-BZT film at the "optimal property point". (A) HAADF-STEM image and (B, C) corresponding GPA analysis of out-of-plane (ε_{yy}) and in-plane (ε_{xx}) normal strain. (D) EDS elemental composite map of Ca (red) and Zr (green) and (E) elemental intensity line profile (raw counts) along the white arrow direction in (D). Scale bars: 10 nm.

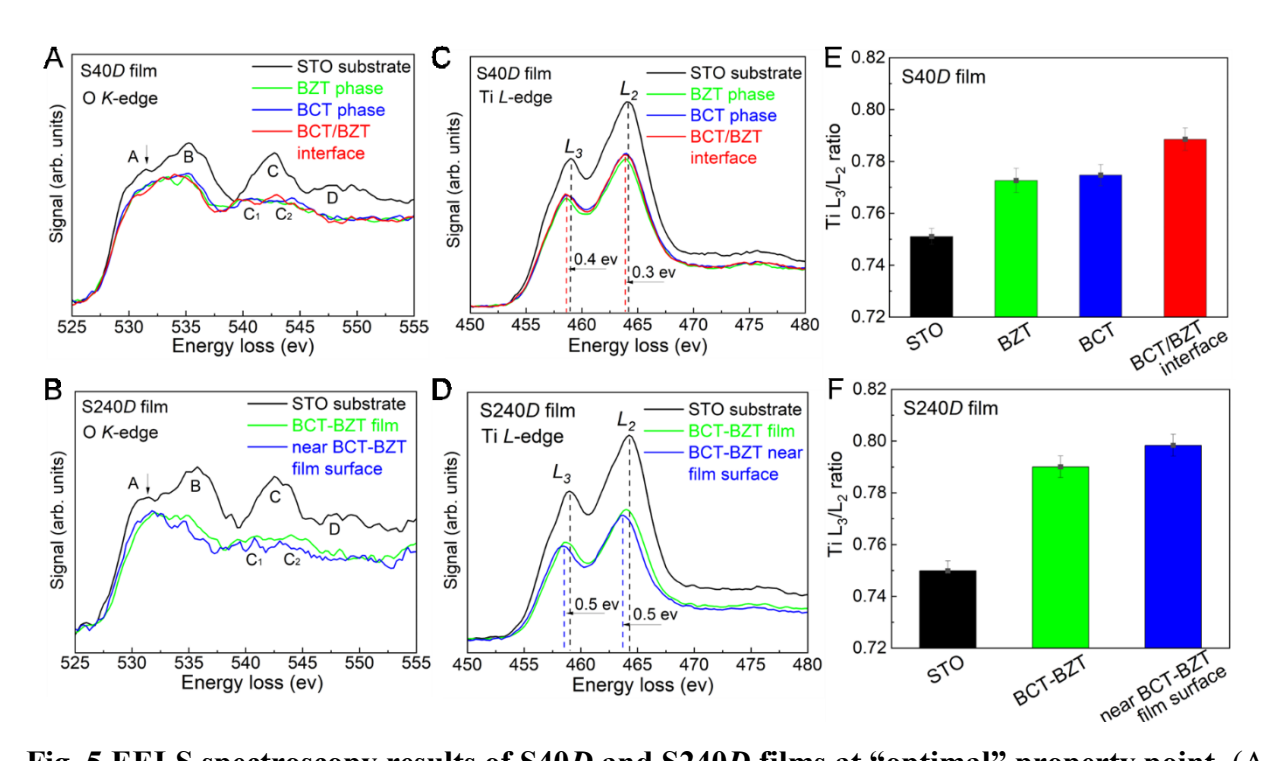


Fig. 5 EELS spectroscopy results of S40D and S240D films at "optimal" property point. (A, B) O K-edges, (C, D) Ti $L_{2,3}$ -edges EELS spectra of S40D and S240D at different locations. (E, F) Ti L_3/L_2 while-line ratios of S40D and S240D films.

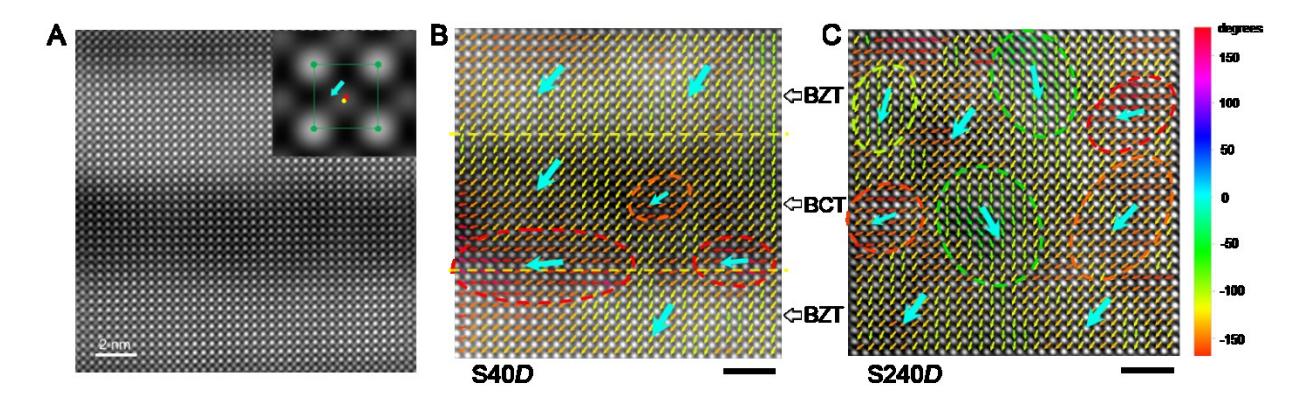


Fig. 6 Polarization displacement vector maps. (**A**) The HAADF-STEM image of BCT-BZT SL film. Inset is a zoom-in view of a single unit cell with the Ba (four corner) and Ti (center) atom positions denoted by green and yellow dots, respectively. The center-of-mass position of the four corner Ba atoms are denoted by a red cross. For the relative shift of Ti atom, the polar displacement vector is denoted by a cyan arrow. Displacement vector map of (**B**) S40*D* and (**C**) S240*D* BCT-BZT thin films. Scale bars: 2 nm.